Available online at www.sciencedirect.com
SCIENCE DIRECT®
International Journal of Heat and Mass Transfer 47 (2004) 1827–1845
International Journal of HEAT and MASS TRANSFER
www.elsevier.com/locate/ijhmt

An experimental study of fluid mechanics and heat transfer in an impinging slot jet flow

V. Narayanan [a,*], J. Seyed-Yagoobi [b], R.H. Page [c]

[a] Department of Mechanical Engineering, Oregon State University, 204 Rogers Hall, Corvallis, OR 97331-6001, USA
[b] Department of Mechanical, Materials, and Aerospace Engineering, Illinois Institute of Technology, 10 W. 32nd Street, Chicago, IL 60616, USA
[c] Department of Mechanical Engineering, Texas A&M University, MS 3123, College Station, TX 77843-3123, USA

Received 4 September 2002; received in revised form 12 October 2003

Abstract

An experimental study of flow field, surface pressure, and heat transfer rates of a submerged, turbulent, slot jet impinging normally on a flat plate is presented. Two nozzle-to-surface spacings of 3.5 and 0.5 nozzle exit hydraulic diameters, which correspond to transitional and potential-core jet impingement, respectively, are considered. Fluid mechanical data include measurements of mean flow field and variance of normal and cross velocity fluctuations, mean surface pressure, and RMS surface pressure fluctuations along the nozzle minor axis. Local heat transfer coefficients are calculated from detailed surface temperature measurements. The heat transfer data follow a trend similar to previous studies, exhibiting high heat transfer rates in the impingement region for transitional jet impingement, and a non-monotonic decay in heat transfer coefficient for potential-core jet impingement. The fluid flow results indicate that past impingement, locations of high streamwise fluctuating velocity variance occur in the wall jet flow for both nozzle spacings. The RMS surface pressure fluctuation profile exhibits a maximum at the impingement line for the transitional jet impingement, and corresponds well with the rise in near-wall velocity fluctuation variance in the free jet prior to impingement. For potential-core jet impingement, the streamwise location of peak RMS pressure fluctuations corresponds to the highly correlated turbulence in the outer region of the wall-bounded flow. Further, there is a good correspondence between the locations of secondary peak in heat transfer and near-wall streamwise fluctuating velocity variance. The occurrence of the outer peak prior to the near-wall peak in streamwise velocity variance for the potential-core jet impingement suggests that the interaction between correlated motion in the outer region and near-wall turbulence causes the rise in heat transfer coefficient towards a secondary peak.

1. Introduction

Impinging jets are used in a wide variety of applications such as cooling of electronics and turbine blades, and in the heating, cooling, or drying of pulp, paper, textile, food, and chemicals. The ability to control heat transfer from the surface by varying flow parameters such as jet exit velocity and flow temperature, and geometrical parameters such as jet exit opening, nozzle-to-surface spacing, and nozzle-to-nozzle spacing in arrays, are some of the key factors that have lead to the sustained and widespread use of jet impingement technologies. The most commonly used geometries are axisymmetric (circular orifice or pipe) and slot (two-dimensional) nozzles.

The flow field of an impinging jet can be divided into three zones: (1) the free jet prior to impingement, (2) the impingement region, and (3) the wall jet region. The free jet region consists of one or more of the following zones depending on the nozzle-to-surface spacing: (1) the potential core, where the jet maintains its exit velocity at the centerline while mixing and diffusing with the ambient fluid in its shear layers; (2) the transition zone, where the core velocity has decayed completely, and the

* Corresponding author.
E-mail address: vinod.narayanan@orst.edu (V. Narayanan).

0017-9310/$ - see front matter © 2003 Elsevier Ltd. All rights reserved.
doi:10.1016/j.ijheatmasstransfer.2003.10.029

Nomenclature

b_o	free jet virtual origin (m)
C_p	pressure coefficient, $C_p = \dfrac{\Delta P_m - \Delta P_{m,ref}}{0.5\rho V_{mo}^2}$
D_h	hydraulic diameter of the nozzle $= 2X_{ws}$ for slot jet (m)
h	heat transfer coefficient (W/m^2 K), $h_{loc} = \dfrac{q''_{net}}{T_h - T_{ad}} = \dfrac{\dfrac{q_{elec} - q_{Cu}}{A_{foil}} - (q''_{rad} + q''_{nc})}{T_h - T_{ad}}$
k	thermal conductivity (W/m K)
L	foil length (m)
$\dot{m}$	mass flow rate (kg/s)
Nu	Nusselt number, $Nu = \dfrac{h_{loc} D_h}{k}$
P	pressure (Pa)
q	heat energy rate (W)
q''	heat energy flux (W/m^2)
r	radial coordinate for a circular (axisymmetric) jet (m)
Re	Reynolds number, $Re = \dfrac{V_{mo} D_h}{\nu}$
T	temperature (°C)
U	time-averaged (mean) velocity in the x-direction (m/s)
u_{RMS}	RMS velocity fluctuation in the x-direction (m/s)
$\langle uu \rangle$	variance of normal velocity fluctuation in x-direction (m/s)^2
$\langle uv \rangle$	variance of cross velocity fluctuation in the x–y plane (m/s)^2
V	time-averaged (mean) velocity in the y-direction (m/s)
V_{max}	time-averaged (mean) velocity along the nozzle centerline at a distance y from the nozzle exit (with reference to Fig. 3) (m/s)
V_{mo}	time-averaged (mean) nozzle exit velocity in the y-direction based on flow rate (m/s)
v_{RMS}	RMS velocity fluctuation in the y-direction (m/s)
$\langle vv \rangle$	variance of normal velocity fluctuation in the y-direction (m/s)^2
X_{ws}	slot width (m)
x	streamwise coordinate along the minor axis of the nozzle; $x = 0.0$ corresponds to the projected nozzle centerline on the impingement surface (m)
Y_n	nozzle-to-surface spacing along the y axis (m)
y	normal (vertical) co-ordinate; $y = 0.0$ location corresponds to the impingement surface, unless otherwise mentioned (m)
z	spanwise coordinate along the major axis of the nozzle; $z = 0.0$ location corresponds to the projected nozzle centerline on the impingement surface minor axis (m)

Greek symbols

Δ	differential
η	non-dimensional geometrical scaling parameter for a free jet, $\eta = \dfrac{x}{y - b_o}$
ρ	density (kg/m^3)

Subscripts

ad	adiabatic
atm	atmospheric
Cu	copper bus bars (heat loss)
elec	electrical
h	heated
loc	local
m	mean value (volume or mass averaged)
max	maximum
nc	natural convection
net	net value of quantity
o	nozzle exit
rad	radiation
ref	reference value of quantity
RMS	root mean square
u	along u velocity direction
v	along v velocity direction
w	along w velocity direction
x	x-direction
y	y-direction
z	z-direction

shear layers interact at the jet centerline; and (3) the fully developed zone, where the jet attains a self-similar behavior. Fig. 1a shows a schematic of a slot jet with the transitional region of the free jet impinging normal to the surface, while Fig. 1b shows the case where the jet potential core impinges on the surface. Typically, the length of the potential core varies between 5 and 6 slot widths from the jet exit, depending on the exit conditions and nozzle geometry [1,2]. Previous studies (for example, [2,3]) have determined that the maximum heat transfer in the impingement region occurs when the transitional jet impinges on the surface.

Table 1 summarizes the experimental studies in a turbulent, subsonic, submerged, single slot jet heat transfer and/or fluid mechanics. Several experimental studies have focused on either the fluid mechanics or heat transfer of impinging axisymmetric or slot jets, but very few have reported on both aspects. Donaldson and

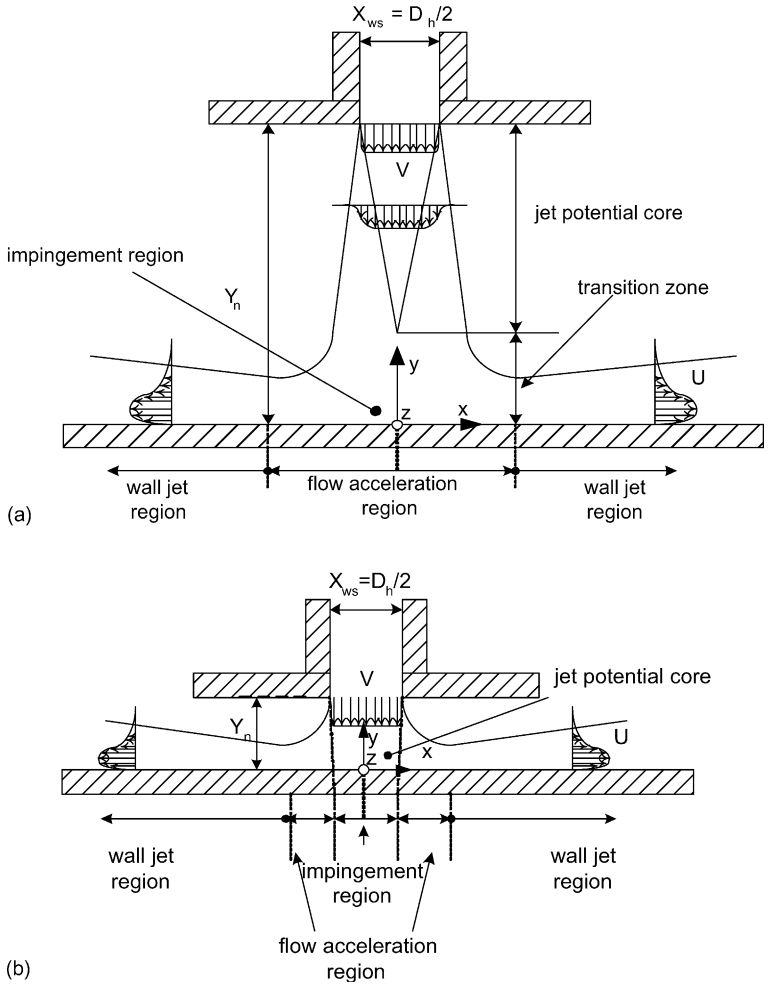

Fig. 1. Schematic of slot jet impingement on a flat surface (a) transitional jet impingement, and (b) potential-core jet impingement.

Snedeker [4], Donaldson et al. [5], Hoogendoorn [6], and Lytle and Webb [7] studied flow field and heat transfer in axisymmetric jets. Donaldson et al. provided fluid mechanical and heat transfer data only for relatively large nozzle-to-surface spacings ($3.5 < D_h < 15$), while Lytle and Webb studied impingement at $Y_n/D < 0.5$. Gardon and Akfirat [2] reported streamwise turbulence intensity in the absence of the impingement surface, along with extensive heat transfer data for impinging slot jets. Yokobori et al. [3,8] studied the behavior of turbulence at the impingement point of two-dimensional and axisymmetric jets, respectively. They confirmed, for transitional jet impingement, the existence of pairs of counter-rotating, large-scale, streamwise vortices at stable nodal locations along the impingement line and discussed their relation with the behavior of upstream shear layer vortices. These coherent structures, they emphasized, were predominant in the transport of heat in the impingement region. Sakakibara et al. [9] reported simultaneous flow field and temperature measurements of a slot jet impinging at a height of 7 slot widths from the surface using particle image velocimetry and laser induced fluorescence techniques.

Many prior studies have reported a non-monotonic trend in local heat transfer coefficient distribution in both axisymmetric and two-dimensional jets at low nozzle-to-surface spacings, ($Y_n/D_h < 2.5$) when the potential core of the free jet impinges on the surface. In circular jet impingement flow at very close nozzle-to-surface spacings, Hoogendoorn [6] and Lytle and Webb [7] showed that the heat transfer coefficient distribution exhibited two peaks away from the stagnation region. The primary peak in the heat transfer distribution occurred near the stagnation point, at $r/D_h = 0.50$, and was attributed to local thinning of the accelerating laminar boundary layer. Hoogendoorn [6] showed that the radial distribution of local streamwise turbulence intensity, measured at the location of maximum radial

Table 1
Summary of experimental fluid mechanic and heat transfer studies on submerged turbulent single slot jets

Investigation	Nozzle geometry (aspect ratio)	Impingement surface, jet incidence	Y_n/D_h	Reynolds number	Measured/calculated quantities	Techniques used
Becko [31]					Literature survey—heat transfer, emphasis on turbine blade cooling	
Martin [1]					Literature survey—mainly heat transfer	
Hrycak [32]					Literature survey	
Looney and Walsh [33]					Literature survey—fluid mechanics, numerical study	
Downs and James [34]					Literature survey—heat transfer	
Polat [35]					Literature survey—process applications	
Viskanta [13]					Literature survey	
Gardon and Akfirat [2,36]	96, 48, 24	Flat, normal	0.25–30	450–50,000	Heat transfer	Heat flux sensor
Korger and Krizek [14]	$X_{ws} = 5$–40 mm	Flat, normal	0.13–20	6040–37,800	Mass transfer	Naphthalene sublimation
Schlunder et al. (Martin [1])		Flat, normal	2.5–10	22,000–93,600	Mass transfer	Evaporation of water
Belatos and Rajaratnam [37]	65	Flat, normal	14.04–67.5	5270–9400	U, V, wall pressure	Preston probe
Gutmark et al. [38]	38.46	Flat, normal	50	30,000	U, V, W, normal and cross Reynolds stress, and turbulence triple products	Cross wire anemometer
Yokobori et al. [3]	10, 30	Flat, normal	1–7.5	2000–20,000	Surface temperature, stagnation vortex pair wavelength and frequency	Thermocouple, hydrogen bubble flow viz.
Striegl and Diller [39]	56.7, 34, 17, 11.3	Flat, normal	3–12.5	3000–40,000	Heat transfer	Heat flux gage
Kataoka et al. [40]	25	Flat, normal		3000–6000	Impingement region flow visualization, heat transfer, and turbulence intensity	Hydrogen bubble flow viz., liquid crystal, two single film sensor anemometry
Kataoka [41]		Flat, normal			Summary of work in flow structures, turbulence, and heat transfer in the impingement region	Hydrogen bubble flow viz., thermocouple, anemometer
Gau and Chung [42]	7.5, 10, 15	Convex and concave, normal	1–8	6000–350,000	Flow visualization, heat transfer	Smoke-wire viz., thermocouple
Gau and Lee [21]	7.5, 12.5, 25, 43	Ribs, normal	1–8	2500–11,000	Flow visualization, heat transfer	Smoke-wire viz., thermocouple
Tu and Wood [27]	61–400	Flat, normal	1–20.6	3040–11,000	Mean wall surface pressure and shear stress	Stanton tube, Preston tube
Sakakibara et al. [9]	10.35	Flat, normal	4	4000	Simultaneous, instantaneous U, V, T_{flow}-focus on stagnation region flow structure	DPIV, LIF

McDaniel and Webb [43]	8, 12, 24	Cylinder, normal	0.5–5.5	600–8000 (based on diameter)	surface averaged heat transfer	Thermocouple
Bietelmal et al. [44]	9.1	Flat, oblique	4–12	4000–12,000	Heat transfer	Thermocouple
Choi et al. [45]	30	Concave, normal	4, 6, 10	1780, 2960, 4740	U, $\langle uu\rangle$, heat transfer	1-D LDA, thermocouple,
Sakakibara et al. [28]	10.35 (fluted nozzle)	Flat, normal	4	4000	instantaneous, statistical and phase averaged planar velocity	DPIV
Zhe and Modi [15]	15	Flat, normal	1–4.6	20,000–60,000	U, V, $\langle uu\rangle$, mean skin friction	Near-wall hot-wire anemometry
Maurel and Solliec [46]	17.5–70	Flat, normal	5–25	6700–110,000	U, V, $\langle uu\rangle$, $\langle uv\rangle$, $\langle uv\rangle$, instantaneous planar flow field	2-D LDA, PIV
Guo and Wood [24]	5.77	Flat, normal	1, 2, 2.5	88,000	Stagnation region normal stresses, mean and fluctuating pressure, $\langle up\rangle$ correlation; mean shear stress profile	Four holed fast response pressure probe
Present study	20	Flat, normal	0.5, 3.5	≈23,000	U, V, $\langle uu\rangle$, $\langle uv\rangle$, $\langle vv\rangle$, P, p, heat transfer, flow visualization	1-D LDA, piezoresistive transducer, IR thermography

velocity, and Nusselt number attained a minimum value at approximately the same radial location for nozzle-to-surface spacings of 2, 4, and 5.9 hydraulic diameters. The minimum in heat transfer coefficient, observed for $Y_n/D_h = 2$ and 4, was attributed to a transition from a laminar to turbulent boundary layer. The secondary peak following this minimum was observed only for cases when a low-turbulence contoured nozzle was used as opposed to a pipe nozzle. Lytle and Webb [7] reported the existence of a secondary peak for a pipe nozzle with a jet turbulence level of around 10% near the impingement region. The location and magnitude of the secondary peak in heat transfer depended on the Reynolds number, nozzle-to-surface spacing, and nozzle geometry. Goldstein et al. [10] attributed the local minimum in the recovery factor distributions at low nozzle spacings to energy separation in the vortex flow. Popiel and Trass [11] performed flow visualization studies on a circular jet impinging at close nozzle-to-surface spacings to qualitatively document the flow behavior. Fox et al. [12] studied the influence of vortex structures on the adiabatic wall temperature distribution in an impinging jet. They showed, by means of an analytical model and experiments, that the wall temperature was modified by the presence of secondary vortex structures that were induced near the plate surface by primary vortices in the outer region. They attributed the region of lower wall temperature at low nozzle-to-surface spacing to secondary vortices. Summarizing results from prior investigations, Viskanta [13] noted that there was considerable speculation and disagreement among researchers as to the explanation behind the secondary peak in heat transfer coefficient. However, in general, the non-monotonic trend in radial distribution of heat transfer coefficients in circular jet impingement at close nozzle-to-surface spacing was attributed to an accelerated laminar boundary layer in the vicinity of the impingement point (primary peak) and the interaction of the large-scale turbulence generated in the mixing layer, and transition to developed turbulent radial wall jet (secondary peak).

Gardon and Akfirat [2] and Korger and Krizek [14] studied the local heat and mass transfer distributions respectively, for potential-core slot impingement at close nozzle-to-surface spacings. Gardon and Akfirat observed a secondary peak in heat transfer coefficient distribution for slot jet impingement at a nozzle-to-surface spacing between 1 and 3 hydraulic diameters, and attributed the peak to a transition from a laminar to a turbulent boundary layer. They also reported a local minimum at the stagnation line, surrounded by primary peaks on either side for a very close spacing of $Y_n/D_h = 0.33$. They proposed that the transition to turbulent flow was triggered by the disappearance of the favorable pressure gradient which existed in the accelerating flow past impingement. The transition resulted in

a rise in local heat transfer coefficients at a $x/D_h = 2$. The rising trend in heat transfer coefficient persisted until the boundary layer thickened to a turbulent profile, along with a decrease in mean flow velocity due to jet spread. These two opposing effects, they speculated, resulted in a secondary peak in heat transfer at a $x/D_h = 3.5$, beyond which heat transfer decreased monotonically. They observed that the non-monotonic variation of heat transfer coefficient was suppressed in the case of high exit jet turbulence intensity. More recently, Zhe and Modi [15] measured mean velocity and turbulence intensity in the near-wall jet flow, and estimated mean wall shear stress on the impingement surface. They observed a secondary peak in mean skin friction around $x/D_h = 2.5$ for three nozzle-to-surface spacings of $Y_n/D_h = 1$, 1.5, and 2. Their study did not include local heat transfer measurements, thereby precluding a discussion on the effect of the wall shear stress on heat transfer distribution.

The primary aim of this paper is to present results of a combined flow field and heat transfer study of a turbulent, submerged, impinging slot jet at the two nozzle-to-surface spacings of interest as highlighted in literature: a spacing of $3.5D_h$ (7.0 jet exit widths), which corresponds to transitional jet impingement, and a spacing of $0.50D_h$ (1.0 jet exit widths), which corresponds to near-wall potential-core impingement on the surface. The exit Reynolds number was 23,400 for flow field measurements, and 22,500 for heat transfer measurements for both nozzle spacings. The paper provides an insight into the distinctly different flow field and heat transport mechanisms that occur during impingement of the jet transitional and potential-core regions. The non-monotonic trend in heat transfer at low spacings is explained based on the flow field, surface pressure, and transient surface temperature results. Further details on transient surface temperature measurements are presented elsewhere [16].

2. Experimental apparatus and instrumentation

Fig. 2a shows a schematic of the jet impingement set-up used in this study. Two dedicated screw compressors located in a separate room supplied compressed air for the jet flow. The air was dried, filtered, and directed into a plenum through two settling tanks and pressure regulators. The mass flow rate was determined using a sonic nozzle at the exit of the last settling tank. The plenum consisted of a honeycomb flow straightener, followed by a series of screens and a convergent section. The jet impingement set-up, shown in Fig. 2a, was located in a large test chamber in order to prevent stray light and other disturbances from affecting the measurements. The flow exited the plenum through an end plate consisting of seven contoured slots of aspect ratio 20:1. The nozzle was attached to the central slot in the plenum, and all other slots were sealed. The geometry of the nozzle used in this study is provided in Fig. 2b. The nozzle width and length were 0.0127 m and 0.102 m, respectively. The nozzle aspect ratio was 20:1 excluding the unconfined, semi-circular ends. A shroud of width $1.20D_h$ on either side from the nozzle centerline was located flush with the nozzle exit, as shown in Figs. 1 and 2b. Preliminary experiments, performed in the absence of the impingement plate, indicated that the exit mean velocity along the major axis of the nozzle, $x = 0.0$, was uniform up to a distance of $z/D_h = \pm 3.5$. In this paper, all flow field, surface pressure, and heat transfer results are reported along the $z/D_h = 0.0$ plane. Two interchangeable impingement plates were used in these experiments: (a) a Plexiglas surface of dimensions 63.5 cm × 73.2 cm for flow field and surface pressure measurements, and (b) a heated inconel impingement surface of dimensions 38.1 cm × 38.1 cm for heat transfer measurements.

Mean flow field and turbulence intensities were measured using a 1-D fiber optic laser Doppler anemometer (LDA) system (TSI Inc.), with collection optics arranged in a backscatter configuration. The probe was traversed in three dimensions by means of an accurate servo motor actuated traverse system with position encoders. A 514.5 nm, 150 mW Argon-ion laser provided the coherent light source. The optic train consisted of a beam splitter, 40 MHz Bragg cell, fiber optic beam launchers, and the transmitting lens within the fiber optic probe. The detected light was focused onto a photo-detector at the end of the fiber optic. The electronics consisted of a frequency downmixer and a signal processor (TSI Inc., model IFA550). Data acquisition and probe traverse was controlled by means of a computer located outside the test chamber. Light-scattering particles for velocity measurement were generated by a mixture of glycol and water, drawn into the air stream due to suction created by an ejector nozzle located in the piping upstream of the plenum entrance. The average size of the particles at the nozzle exit was estimated to be between 3 and 5 μm in diameter.

Local surface temperatures were measured non-intrusively with an 8–13 μm wavelength infrared (IR) camera (Mikron Inc., model 6T62 thermotracer). The temperature resolution of the camera in the normal mode of operation was 0.1 °C, and as high as 0.025 °C in the high signal-to-noise improvement mode. The camera optics in front of the single cooled detector scanned the field of view for temperatures over 256 × 206 spatial locations. The camera was placed in a vented enclosure directly below the foil (see Fig. 2a). The temperature rise in the enclosure did not exceed 1 °C during the test duration of approximately 5 h. The heat transfer impingement surface consisted of a central constant heat flux surface surrounded by Plexiglas end plates on all sides. The entire test section was 63.5 cm long × 63.5 cm

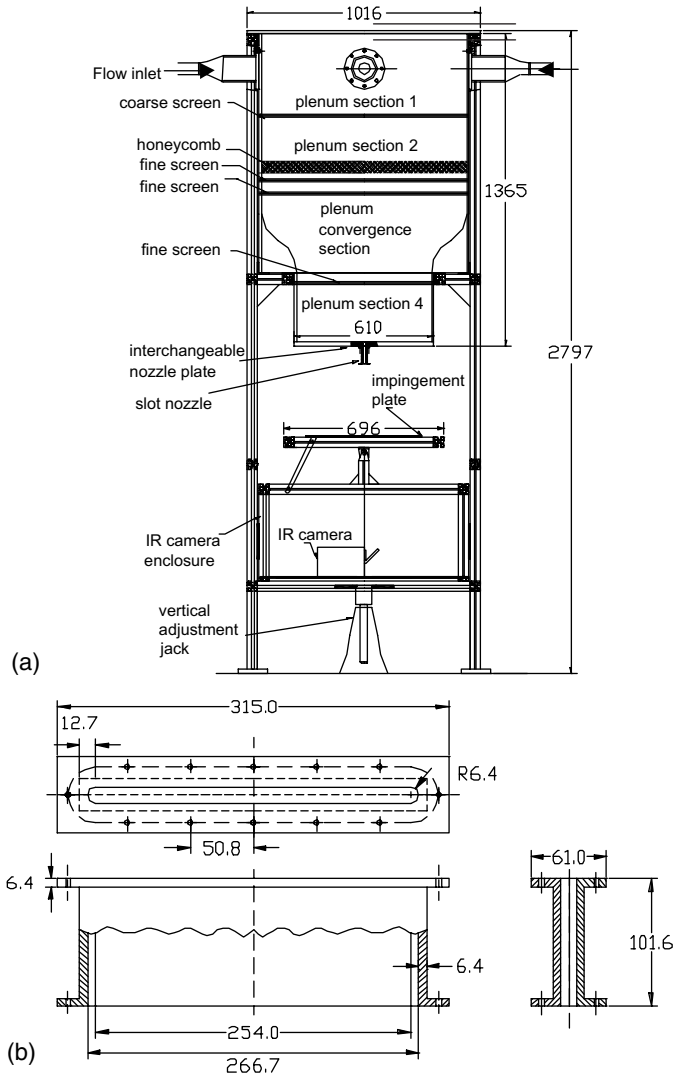

Fig. 2. Schematics of the (a) jet impingement facility and (b) nozzle geometry. All dimensions are in mm.

wide. The central heat transfer test section consisted of a 0.0254 mm thick Inconel 600 foil 38.1 cm long $\times$ 38.1 cm wide, stretched tightly between two solid copper bus bars. The foil was electrically heated by means of a high current DC power supply to provide a constant heat flux surface. Solid copper rods were used to transmit power to the bus bars. Voltage difference was measured at the bus bars, and the electrical contact resistance between the foil and bus bars was considered while determining the net voltage drop across the foil. Current through the foil was measured at the power supply readout. The underside of the foil and the surrounding Plexiglas surface was coated with flat black paint to provide a constant high emissivity, diffuse surface for radiation detection. The emissivity of the painted foil surface was determined to be 0.96, based on ambient temperature calibration of the IR camera with respect to a calibrated thermistor located on the foil surface. This value was not expected to change considerably with temperature, since the foil was heated to less than 15 °C above ambient temperature.

Mean and fluctuating wall pressures were measured using a piezoresistive differential pressure transducer (Kulite Semiconductor Products, Inc., model XCS062). The transducer had a pressure sensitive diameter of 0.71 mm, and was mounted flush with the surface. The transducer output signal was amplified and low-pass filtered at 20 kHz, using a strain gage amplifier module (Encore Electronics, model 619M). For mean pressure measurements, the output voltage from the amplifier was directly read by a high-resolution digital multimeter (Hewlett Packard, model 3478A) and recorded through

a GPIB interface onto a PC. For RMS pressure measurements, the voltage data was high-pass filtered at 0.01 Hz. A 12-bit data acquisition board (National Instruments, model 6024E) was used to further amplify and digitize the signal. In order to obtain pressure profiles, the surface (and correspondingly, the sensor) was traversed along the x-direction by means of a computer controlled traverse system.

3. Data collection and analysis procedure

LDA measurements were obtained with three different rotary orientations of the probe in order to estimate the mean velocity and streamwise, normal, and cross fluctuating velocity variance at each location using a component resolution technique [17,18]. Preliminary experiments indicated that the flow measurements remained unchanged between experimental runs. An estimated repeatability in the measurement volume coincidence to within ±0.1, ±0.1, and ±0.25 mm, in the x, y, and z directions respectively, between the three probe rotary orientations was achieved by consistent alignment procedures. Five thousand data points were recorded at each location in the flow field, and analyzed to obtain mean flow and turbulence quantities. A transit-time-weighting technique was used to eliminate velocity bias.

During a typical heat transfer experiment, eight consecutive temperature maps of the unheated foil with jet impingement were obtained at steady state, and averaged in order to estimate the mean local adiabatic foil temperatures. The foil was then heated and the temperature distribution measured after steady state temperature was attained. Again, eight consecutive frames were averaged to obtain a mean local heated temperature distribution on the foil. The heat flux to the foil was measured through the voltage and current readings, and the known heated foil area. Heat losses due to radiation and natural convection from both the upper and lower surfaces of the foil, and end conduction to the copper bus bars were taken into consideration while calculating the net heat flux at each pixel location. For the radiation loss calculation from the upper side of the foil, a constant emissivity of 0.10 was used from literature [19], based on the normal total emissivity value for a 0.0254 mm polished Inconel foil at 300 K. The local heat transfer coefficient was determined from the net heat flux and the local temperature difference between the heated and unheated foil.

The surface pressure experiments consisted of traversing the impingement surface with the piezoresistive transducer along the minor axis of the nozzle, $z/D_h = 0.0$. At each location, dc voltage readings for the mean pressure, followed by ac voltage readings of the pressure fluctuations were obtained. This procedure eliminated any position-related uncertainty between the mean and RMS fluctuating pressure data. An average of 300 samples of dc voltage readings from the voltmeter was used to determine the mean pressure differential. For the fluctuating component, two million data points were recorded through the data acquisition card at a sampling rate of 60 kHz. To prevent aliasing effects, the signal was low-pass filtered at 20 kHz in the amplifier module prior to digitization of the signal.

Uncertainties in reported data were calculated based on propagation of errors method [20] and are presented in Table 2. The velocity profile at the slot exit was integrated to obtain a mass balance. The mass flow rate was found to agree to within 3% of the flow rate calculated by the flowmeters. Table 3 provides a comparison of local Nusselt numbers, Nu_{loc}, determined in the present study with data from literature for a slot jet under similar Reynolds numbers and nozzle spacings.

Table 2
Uncertainty estimates for fluid mechanics and heat transfer data

Variable	Percent uncertainty
Mass flow rate, $\dot{m}$ (kg/s)	1.5%
Mean velocity, U (m/s) (calculated)	2.7% of local velocity
Mean velocity, V (m/s) (measured)	2.7% of local velocity
Fluctuating velocity variance, $\langle uu \rangle$ (m^2/s^2) (calculated)	Maximum of 15% of local $\langle uu \rangle$, typically less than 10% in near-wall regions, and less than 5% at $y/D_h > 0.15$
Fluctuating velocity variance, $\langle vv \rangle$ (m^2/s^2) (measured)	Maximum of 13.7% of local $\langle vv \rangle$, typically <10% near the wall in the high-velocity regions, and less than 2% at $y/D_h > 0.15$
Fluctuating velocity variance, $-\langle uv \rangle$ (m^2/s^2) (calculated)	Typically less than 20% of local $\langle uv \rangle$ for near-wall measurements, and less than 10% at $y/D_h > 0.15$
Pressure coefficient	8.7% for $C_{p,max}$
RMS surface fluctuating pressure (Pa)	10% of $\Delta P_{RMS,max}$
Heat transfer coefficient, Nu_{loc}	maximum of 7.1% of Nu_{loc}, with an average of 5.0% of Nu_{loc}
Pixel location uncertainty in temperature measurements	1.5% of 1 pixel value

Table 3
Comparison of Nu_{loc} between present experiments and literature

x/D_h	0	1	2	3	4	5
1. Present data[a]	145	101.2	76.3	69.5	64.2	57
2. Schlunder et al. (Martin [1])[b]	145	89	72.5	62	56	51.5
% difference (1−2)/[(1+2)/2]	0.0	12.9	5.2	11.4	13.7	10.1

[a] $Re = 22,500$, $Y_n/D_h = 3.5$.
[b] $Re = 22,000$, $Y_n/D_h = 4.0$.

The present data are in fairly good agreement with those of Schlunder et al. (reported in [1]).

Uncertainties in mean flow velocity and fluctuating velocity variance were calculated at each measurement location. Typical uncertainties in the measured mean and fluctuating velocity variance for the slot jet at $Y_n/D_h = 0.5$ are provided in Table 2. Uncertainties in the measured mean values were less than 3% in all cases, while that in the measured fluctuating velocity variance were as large as 13.7% at near-wall locations with a large mean velocity component. The velocity uncertainty estimate includes errors due to the uncertainty in fringe spacing and the clock resolution of the processor. The uncertainties in the calculated quantities, U, $\langle uu\rangle$, $\langle uv\rangle$ were based on the component resolution equations, and were typically larger than those in quantities that were directly measured (V and $\langle vv\rangle$).

For surface pressure measurements, the transducer, amplifier, and data acquisition board were calibrated as a single unit in the range of measurement using a micromanometer as the reference. The electronics were kept on for the entire duration of the experiments to prevent any errors due to thermal drift in the electronics for both flow field and surface pressure measurements. Although the response of the pressure transducer was linear, base readings (with no air flow) taken prior to the experimental run and after the experimental run exhibited a slight zero drift. This introduced an uncertainty in the mean pressure measurements alone, since the ac values were high-pass filtered prior to data acquisition. To account for the zero drift, for each experiment, two (base) pressure measurements were obtained with no flow—the first prior to the experiment and the second on completion of the experiment. The pressure measurements at each location were subtracted from these base readings, and the mean of the two readings was taken to be indicative of the pressure differential at that location. This method of taking a difference in voltages between the measured location and the base also eliminated any zero offset of the transducer recorded under no flow condition. Typical resolution for the mean pressure measurements with the multimeter was as high as 0.08% of the maximum measured pressure.

4. Results and discussion

4.1. Flow field

Fig. 3a and b present results from free jet experiments at an exit Reynolds number of 35,000. In these figures, the x- and y-coordinates represent the streamwise and

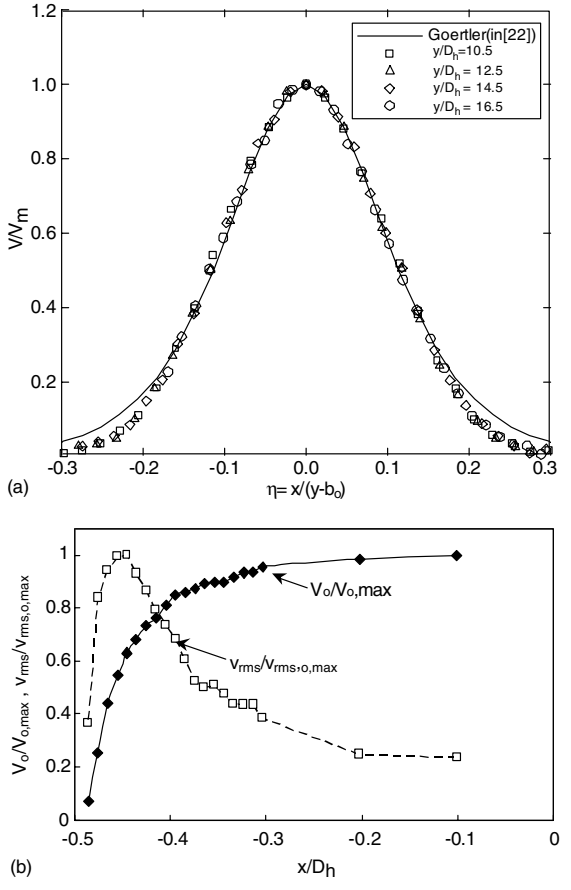

Fig. 3. Preliminary free jet results. (a) Mean non-dimensional velocity profiles of the slot jet in the similarity region, and (b) mean non-dimensional exit velocity and turbulence intensity profiles at $z = 0$. An $x/D_h = 0$ corresponds to the jet centerline, and a $v_{RMS}/v_{RMS,o,max} = 0.2$ corresponds to 3.5% turbulence intensity at the jet centerline.

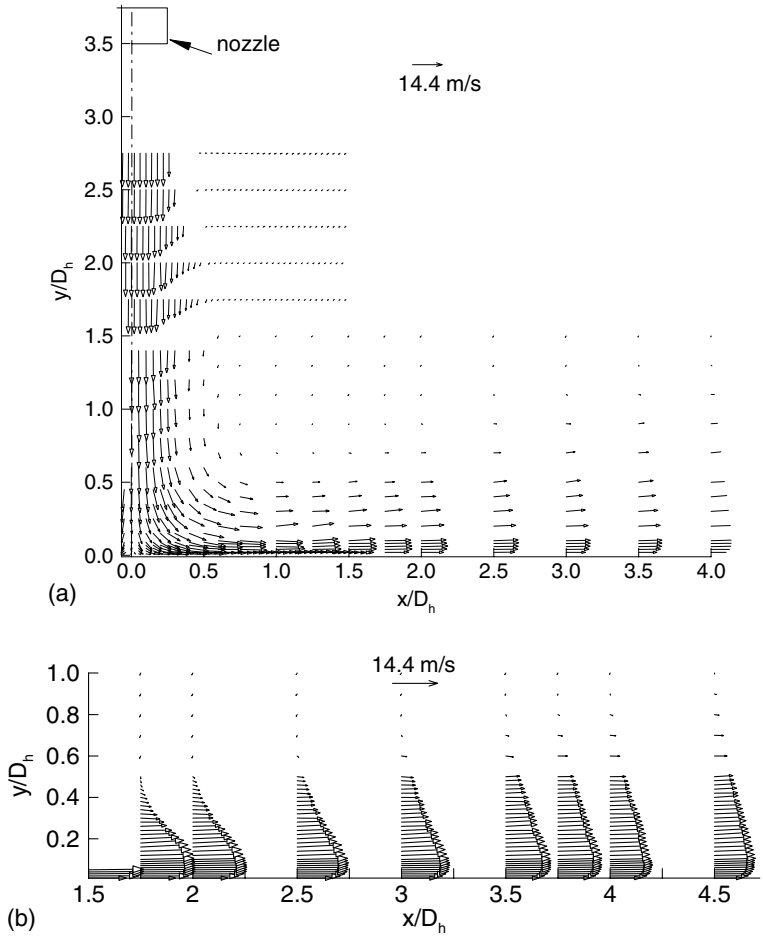

Fig. 4. Plots of the mean velocity field in a slot jet flow. (a) $Y_n/D_h = 3.0$ and (b) $Y_n/D_h = 0.50$.

lateral direction, respectively. The origin of the coordinate system is at the nozzle exit. Fig. 3a shows profiles of the dimensionless mean velocity, V, normalized by the local jet centerline velocity, V_{max}, for the free jet at four streamwise locations. The mean velocity profiles exhibited a self-similar behavior, collapsing onto a single curve past $y/D_h = 10.5$ from the nozzle exit. The solid line represents Goertler's semi-analytical solution for a free jet (presented in [22]), with a spread parameter of 7.67. Fig. 3b shows the dimensionless mean velocity and turbulence intensity profile at the jet exit. The average exit RMS velocity fluctuation in the streamwise direction was 3.5% of the mean jet exit velocity.

Figs. 4–7 present flow field results of slot jet impingement at the two nozzle spacings of $Y_n/D_h = 3.5$ and 0.50. The axis representation and relevant geometrical parameters are indicated in Fig. 1a and b. Mean velocity components were made non-dimensional with the mean exit velocity while the fluctuating velocity variance was made non-dimensional with the square of the mean exit velocity. The exit Reynolds number, based on the nozzle hydraulic diameter is 23,400. Flow field in regions of the free jet near the nozzle exit could not be determined due to obstruction of the beam by the nozzle walls.

Fig. 4a show the mean flow velocity vectors of the slot jet flow field for the nozzle spacing of $Y_n/D_h = 3.50$. The potential core of the jet extended between 5 and 5.5 slot widths from the nozzle exit. The mean flow kinetic energy was high in the potential core up to around $y/D_h = 0.8$, after which the flow rapidly decelerated to zero normal velocity at the impingement point. Beyond $x/D_h = 1.00$, the developing wall jet flow showed deceleration due to a spread of momentum normal to the surface. Fig. 4b shows the mean flow velocity vectors of the slot jet flow field for the nozzle spacing of $Y_n/D_h = 0.50$. The kinetic energy of the mean flow at the first detailed measurement location of $x/D_h = 1.75$ was concentrated in y/D_h locations below 0.15, indicating that the high-velocity region of the wall-bounded flow

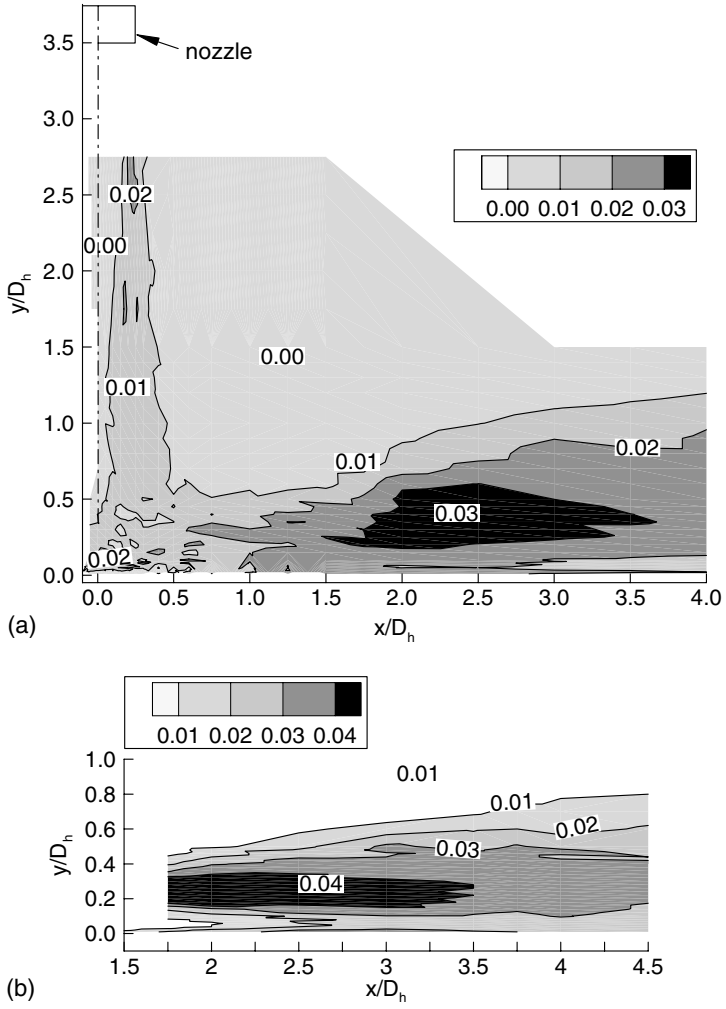

Fig. 5. Contour plot of the non-dimensional x-direction fluctuating velocity variance, $\langle uu\rangle/V_{\mathrm{mo}}^2$, in a slot jet flow. (a) $Y_n/D_{\mathrm{h}} = 3.50$ and (b) $Y_n/D_{\mathrm{h}} = 0.50$.

was not in contact with the shroud. Flow visualization studies of Popiel and Trass [11] demonstrated that for a jet impinging at $Y_n/D_{\mathrm{h}} = 1.2$, the presence of a shroud, extending to 33 cm around the circular nozzle exit, did not significantly impact the vortex filament pattern in the outer region of the wall boundary layer. Near-wall flow acceleration persisted up to about $x/D_{\mathrm{h}} = 1.50$, where a peak $U/V_{\mathrm{mo}} = 1.2$ was measured at $y/D_{\mathrm{h}} = 0.03$.

Fig. 5a presents a contour plot of the non-dimensional velocity fluctuation variance parallel to the impingement surface, $\langle uu\rangle/V_{\mathrm{mo}}^2$, for the slot jet at $Y_n/D_{\mathrm{h}} = 3.50$. The variance was high in the shear layers of the free jet close to the nozzle exit, and in the outer mixing region of the wall-bounded flow past impingement. In the free jet region prior to impingement, the shear layers spread with progression downstream, reducing the extent of the potential core. At $y/D_{\mathrm{h}} \approx 0.09$ above the impingement line, the stress exhibited a local high value at the jet centerline, before being damped by the presence of the wall. Past impingement, $\langle uu\rangle/V_{\mathrm{mo}}^2$ reached a maximum value of 0.037 in the outer region of the developing boundary layer at $x/D_{\mathrm{h}} = 2.0$ and $y/D_{\mathrm{h}} = 0.30$. The nearest-wall $\langle uu\rangle/V_{\mathrm{mo}}^2$ attained a maximum value of 0.030 at $x/D_{\mathrm{h}} \approx 1.5$. Fig. 5b presents $\langle uu\rangle/V_{\mathrm{mo}}^2$ contours for the slot jet at $Y_n/D_{\mathrm{h}} = 0.50$. Regions of high-turbulence intensity were located in the outer shear layer between the wall jet and the ambient surrounding fluid. Past impingement, $\langle uu\rangle$ in the outer mixing layer was higher compared the larger nozzle spacing. The nearest-wall measurement of $\langle uu\rangle$ peaked at $x/D_{\mathrm{h}} \approx 3.0$.

The contour of the non-dimensional y-direction component of the fluctuating velocity variance, $\langle vv\rangle/V_{\mathrm{mo}}^2$, for the slot jet at $Y_n/D_{\mathrm{h}} = 3.50$ is shown in

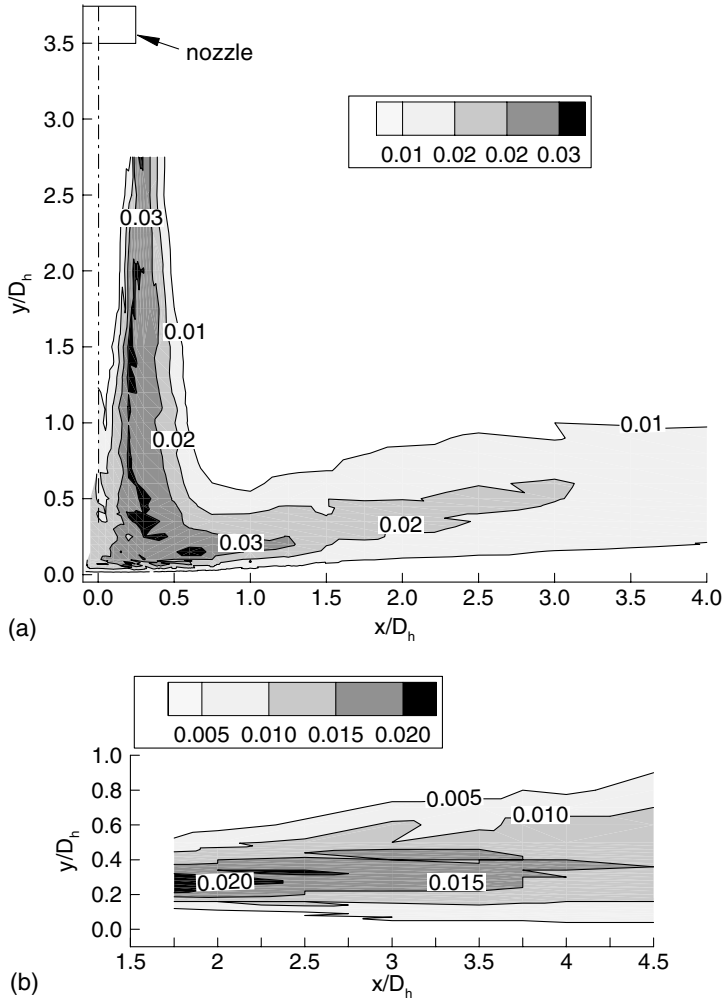

Fig. 6. Contour plot of the non-dimensional y-direction fluctuating velocity variance, $\langle vv\rangle/V_{\mathrm{mo}}^2$, in a slot jet flow. (a) $Y_n/D_{\mathrm{h}} = 3.50$ and (b) $Y_n/D_{\mathrm{h}} = 0.50$.

Fig. 6a. High values of $\langle vv\rangle/V_{\mathrm{mo}}^2$ in the free jet shear layer, with a lateral spread with increasing distance downstream from the nozzle exit were observed. In the measured region of the flow, a maximum $\langle vv\rangle/V_{\mathrm{mo}}^2$ of 0.038 occurred at $y/D_{\mathrm{h}} = 2.75$ and $x/D_{\mathrm{h}} = 0.30$. Past impingement, $\langle vv\rangle/V_{\mathrm{mo}}^2$ was high in the initial part of the developing wall-bounded flow between $y/D_{\mathrm{h}} = 0.15$ to 0.25 and $x/D_{\mathrm{h}} = 0.25$ to 1.0, where a large streamwise mean flow velocity gradient existed. In contrast, as seen in Fig. 5a, $\langle uu\rangle/V_{\mathrm{mo}}^2$ attained a maximum value in the outer wall-bounded flow significantly later, at $x/D_{\mathrm{h}} \approx 2.0$. In contrast, for the $Y_n/D_{\mathrm{h}} = 0.50$ spacing shown in Fig. 6b, $\langle vv\rangle/V_{\mathrm{mo}}^2$ in the outer region exhibited high values at the same locations as the streamwise component, $\langle uu\rangle/V_{\mathrm{mo}}^2$ (see Fig. 5b). The magnitude of peak $\langle vv\rangle$ was around 45% of the peak $\langle uu\rangle$ in the outer shear layer of the wall jet. For a free shear flow, a value of $\langle uu\rangle$ approximately twice that of $\langle vv\rangle$ is expected, since production of turbulence kinetic energy from the mean flow occurs solely in the transport equation for $\langle uu\rangle$. The normal velocity fluctuation receives its energy through a redistribution of turbulent kinetic energy by fluctuating pressure and velocity gradient interactions [23].

Fig. 7a shows a plot of the non-dimensional x–y (cross) component of the fluctuating velocity variance, $-\langle uv\rangle/V_{\mathrm{mo}}^2$, for the slot jet at $Y_n/D_{\mathrm{h}} = 3.50$. A high positive value in the shear layer of the developing free jet near the nozzle exit was observed, while the outer region of the developing boundary layer showed an equally high negative value. The opposing signs of mean velocity gradient and fluctuating cross velocity variances indicated a net generation of turbulence at both locations. Fig. 7b shows a plot of $-\langle uv\rangle/V_{\mathrm{mo}}^2$ for the slot jet at

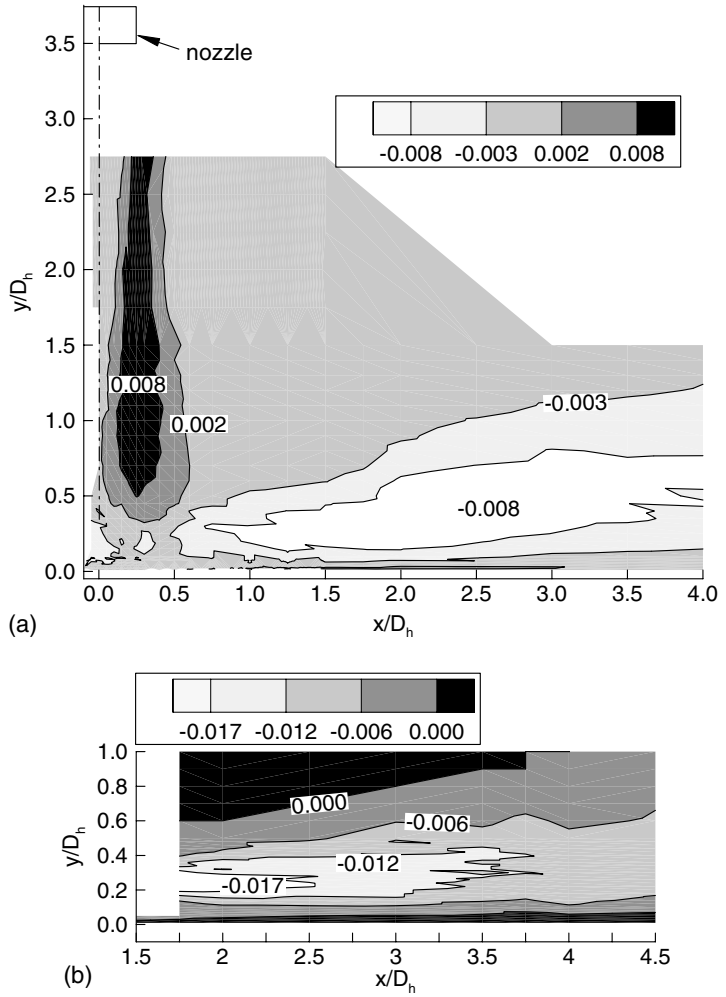

Fig. 7. Contour plot of the non-dimensional x–y component of fluctuating velocity variance, $-\langle uv\rangle/V_{\mathrm{mo}}^2$, in a slot jet flow. (a) $Y_n/D_{\mathrm{h}} = 3.50$ and (b) $Y_n/D_{\mathrm{h}} = 0.50$.

$Y_n/D_{\mathrm{h}} = 0.50$. Large negative value of fluctuating cross velocity variance was observed in the outer mixing layer, similar to the transitional jet impingement (Fig. 7a). High values of mean streamwise velocity gradient normal to the wall, $\partial U/\partial y$, and fluctuating cross velocity variance indicated a production of turbulence in this region.

4.2. Heat transfer

Two-dimensional contours of local heat transfer coefficient for the slot jet nozzle at a turbulent exit Reynolds number of 22,500 were determined from local surface temperature distribution for nozzle-to-surface spacings between Y_n/D_{h} of 0.5 and 5.0. Although the slot jet nozzle used in this study was not confined at its ends, the contour plots of local heat transfer for largest spacing of $Y_n/D_{\mathrm{h}} = 5.0$ indicated two-dimensionality around the centerline, $z/D_{\mathrm{h}} = 0.0$. The heat transfer results are typical of those reported in jet literature [1,2]. Figs. 8a and 9a present dimensionless plots of local heat transfer coefficient, Nu_{loc}, for $Y_n/D_{\mathrm{h}} = 3.50$ and 0.50, respectively, as a function of streamwise distance from the impingement line. For $Y_n/D_{\mathrm{h}} = 3.5$, the heat transfer coefficient decreased monotonically with increasing distance from the jet centerline, with a change (reduction) in negative gradient at $x/D_{\mathrm{h}} = 1.5$. For spacings of $Y_n/D_{\mathrm{h}} < 2.5$, a non-monotonic decay in Nu_{loc} distribution was observed with a primary peak at the impingement line, followed by a secondary peak that occurred closer to the nozzle centerline with reduced nozzle-to-surface spacing. In particular, for the $Y_n/D_{\mathrm{h}} = 0.5$ slot jet impingement (see Fig. 9a), a region of low heat transfer was observed at $x/D_{\mathrm{h}} = 1.6$, followed by a secondary peak region further downstream at $x/D_{\mathrm{h}} = 3.2$.

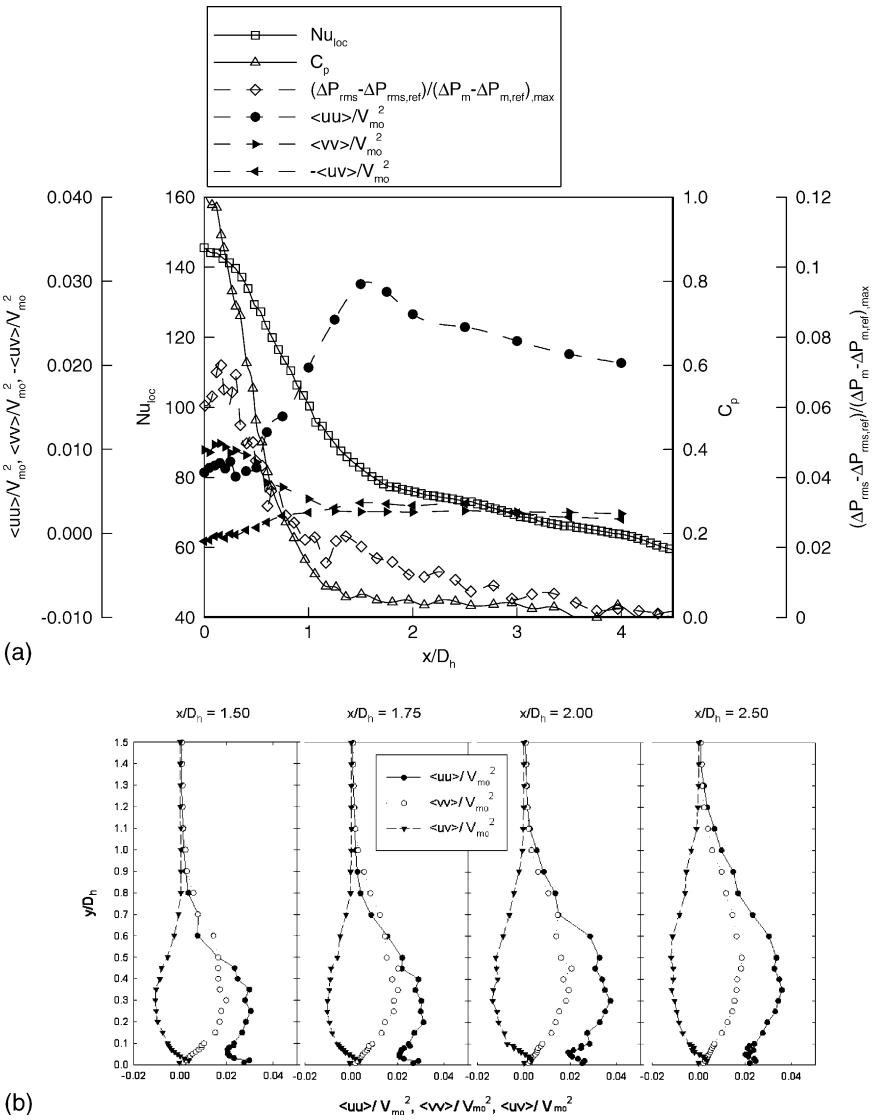

Fig. 8. (a) Combined plot of dimensionless heat transfer coefficient, mean and RMS pressure, and near-wall fluctuating velocity variance distributions on impingement surface for the $Y_n/D_h = 3.5$ slot jet nozzle along the minor axis of the nozzle, at centerline, $z/D_h = 0.00$. (b) Dimensionless fluctuating velocity variance profiles at four locations along the wall-bounded flow of the slot jet at $Y_n/D_h = 3.50$.

The variation of impingement region heat transfer coefficient with nozzle spacing observed in the present study was very similar to that observed by Gardon and Akfirat [2]. They reported a non-monotonic trend in the impingement line heat transfer coefficient at $Re = 22,000$ with an increase for spacings lower than $Y_n/D_h < 1$. The present study indicated that the inflexion occurred at a slightly higher spacing between $Y_n/D_h = 1.0$ and 1.5 [25]. The peak impingement line Nusselt number occurred between nozzle spacings of $Y_n/D_h = 3.5$ and 4.0. The non-monotonic trend in impingement line heat transfer coefficient with nozzle spacing has been attributed to opposing effects of increased turbulence with increase in Y_n/D_h, and a declining centerline velocity beyond the potential core of the jet [2]. The impingement point Nusselt number was greater by 39% for $Y_n/D_h = 3.50$, and by 6.3% for $Y_n/D_h = 0.50$, when compared with the analytical laminar stagnation flow heat transfer solution [26].

4.3. Discussion

Figs. 8a and 9a represent combined non-dimensional plots of the local heat transfer coefficient, mean surface

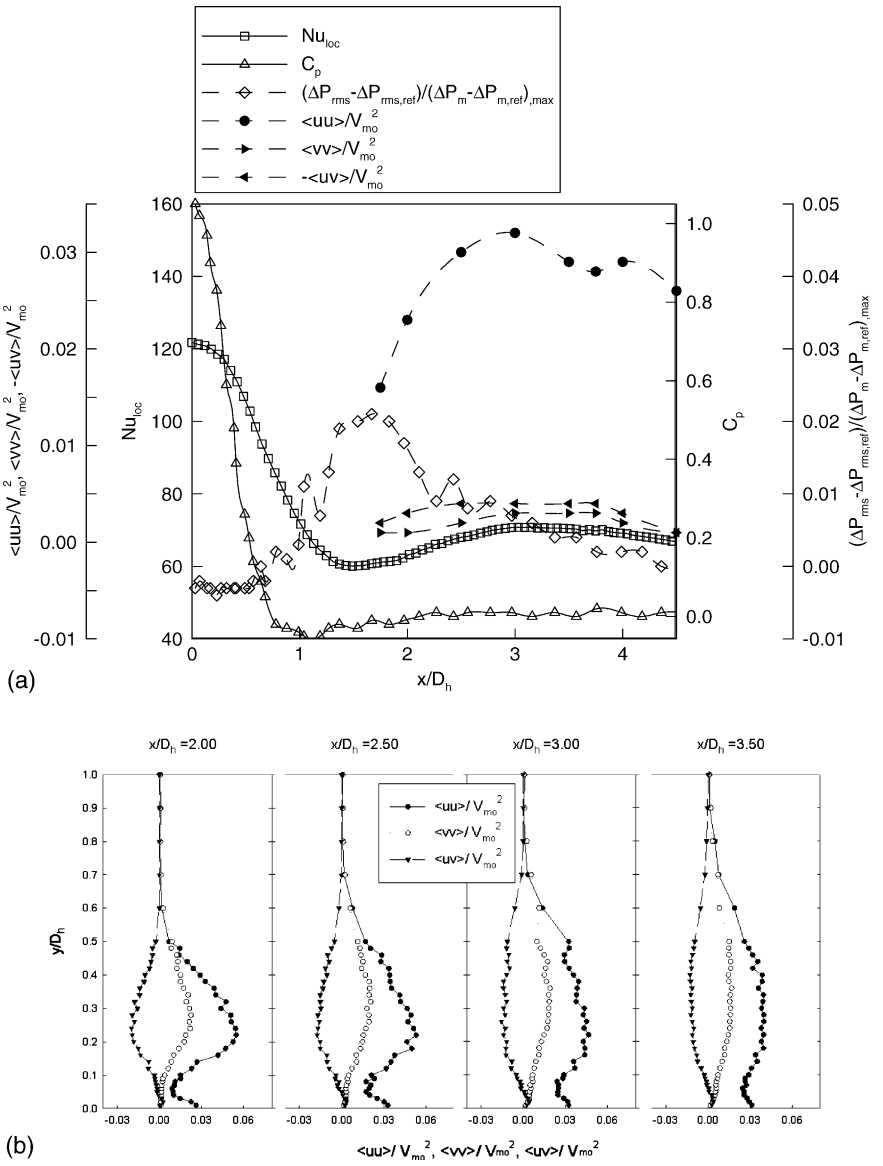

Fig. 9. (a) Combined plot of dimensionless heat transfer coefficient, mean and RMS pressure, and near-wall fluctuating velocity variance distributions on impingement surface for the $Y_n/D_h = 0.5$ slot jet nozzle along the minor axis of the nozzle, at centerline, $z/D_h = 0.00$. (b) Dimensionless fluctuating velocity variance profiles at four locations along the wall-bounded flow of the slot jet at $Y_n/D_h = 0.50$.

pressure, RMS surface pressure fluctuation, and near-wall fluctuating velocity variances along the minor axis for $Y_n/D_h = 3.5$ and 0.5, respectively. The near-wall fluctuating velocity variances reported in this figure corresponded to a physical location of $y/D_h = 0.02$. The mean surface pressure at each location was subtracted from a reference pressure measured at a downstream reference location of $x/D_h = 4.5$, and is represented as a pressure coefficient, C_p. The RMS surface pressure fluctuation was also subtracted from its reference value, and normalized with the peak mean pressure differential.

For $Y_n/D_h = 3.5$, the mean pressure exhibited a Gaussian distribution, as reported in several prior studies (for example, [13,27]). The peak values of Nu_{loc} and C_p occurred at the impingement location. The peak RMS pressure fluctuation occurred in the impingement region and extended to approximately $0.4D_h$ on either side of the jet centerline, followed by a monotonic decrease downstream. High RMS pressure fluctuation around the impingement region indicated significant unsteadiness in the jet flow approaching the impingement region, and can be attributed to the high near-wall

$\langle vv \rangle$ and $\langle uu \rangle$ of the jet prior to impingement. High $\langle uu \rangle$ and $\langle vv \rangle$ at a location of $y/D_h \approx 0.1$ in the free jet above the impingement location were attributed primarily to turbulent transport by convection from the free jet mixing region to the centerline, and to turbulence production caused by the high mean streamwise velocity gradient, $\partial V/\partial y$, near the impingement region.

Prior studies (for example, [3,9,28]) have observed, by flow visualization and detailed PIV measurements, the presence of stable streamwise vortex pairs along the stagnation line for transitional jet impingement, and have attributed the enhanced heat transfer in this region to their presence. In this study, the presence of, and interaction between the vortex filaments was deduced through temporal wall temperature measurements at discrete $x/D_h =$ constant lines, and are detailed elsewhere [16]. For a transitional jet impingement ($Y_n/D_h = 5.0$), results indicated the presence of warm and cold thermal streaks that meandered in time about discrete spatial z-locations at the impingement line, $x/D_h = 0.0$. These streaks persisted beyond the impingement region, and existed at a downstream location of $x/D_h = 1.19$. A conceptual sketch of flow patterns based on flow field studies of other researchers (for example, [3,9]) suggested that the hot streaks corresponded to the location of the counter-rotating vortex pair, while the cold streaks corresponded to the region between, where the jet impinged directly on the wall. RMS temperature fluctuation data exhibited high values at locations between the hot and cold streaks, and were attributed to the unsteady motion of the vortex pairs.

Past impingement, $\langle vv \rangle$ peaked in the outer mixing region, between $x/D_h = 0.25$ and 1.00, (see Fig. 6a) prior to the $\langle uu \rangle$ peak that occurred around $x/D_h = 2.0$ (see Fig. 5a). The fluctuating cross component of velocity variance, $\langle uv \rangle$, also peaked in the outer region at around $x/D_h = 2.0$ (Fig. 7a). The region of high $\langle uu \rangle$ in the outer layer persisted up to $x/D_h \approx 3.0$, followed by a decline, primarily due to a reduction in mean flow kinetic energy. In the inner region of the developing flow past reattachment, $\langle uu \rangle$ peaked between $x/D_h = 1.25$ and 1.50, prior to the location of the outer region peak further downstream at $x/D_h = 2.0$. Fluctuating velocity variance profiles at four locations between $x/D_h = 1.50$ and 2.50, shown in Fig. 8b, indicated the development of a region of increased $\langle uu \rangle$ in the outer mixing layer, along with a diminution of its value in the near-wall region with distance downstream of impingement. From Fig. 8a, the near-wall $\langle uu \rangle$ gradient exhibited a positive slope from $x/D_h \approx 0.5$ to 1.5, while the RMS fluctuating pressure gradient showed a negative slope in the same region, suggesting an inverse correlation between the streamwise gradients of RMS pressure fluctuation and near-wall $\langle uu \rangle$. Kataoka et al. [29] reported local mass transfer rate, velocity gradient fluctuations, and surface pressure fluctuations on a turbulent axisymmetric impinging jet. They found high surface pressure fluctuations at the impingement point and attributed it to the velocity turbulence of the oncoming jet. They indicated that, in turn, the surface pressure fluctuations produced radial velocity disturbances in the wall region of the momentum boundary layer.

For $Y_n/D_h = 0.50$ jet impingement, the combined fluid mechanics and heat transfer plot shown in Fig. 9a indicates that the mean surface pressure and local heat transfer coefficient peaked in the impingement region. The RMS pressure fluctuation in the impingement region was lower than at the reference location downstream, as indicated by the slight negative value of the non-dimensional RMS pressure profile. Although turbulence in the flow field was not measured directly beneath the nozzle, the low values of RMS pressure fluctuation indicated that a low-turbulence potential core of the jet impinged on the surface. As mentioned before, the heat transfer coefficient at the impingement line differed by only 6.3% from the analytical laminar flow solution. The high mean streamwise velocity gradient, $\partial V/\partial y$, of the free jet prior to impingement was not accompanied by high near-wall turbulence (deduced from the measured RMS pressure fluctuations), suggesting an absence of significant levels of turbulence production in the near-wall impingement region at this nozzle spacing. Time trace of wall surface temperature and RMS temperature fluctuations [16] indicated little unsteadiness at the impingement line, suggesting the absence of streamwise counter-rotating vortex pairs at this spacing.

In Fig. 5b, for the range of flow measurements, the maximum $\langle uu \rangle$ in the outer region occurred at $x/D_h = 1.75$. Since this was the first downstream location of detailed measurements, it was unclear if a higher $\langle uu \rangle$ existed prior to this location. The peak $\langle vv \rangle$ and $\langle uv \rangle$ in the outer shear layer also occurred in this region (see Figs. 6b and 7b), and there was a high correlation between the turbulent fluctuations.

From Fig. 9a, the favorable gradient of mean surface pressure was larger than for transitional jet impingement, indicating stronger flow acceleration up to $x/D_h \approx 0.8$. The RMS pressure fluctuation increased past $x/D_h = 0.8$, and peaked around $x/D_h = 1.50$–1.75 in the region of high turbulence in the outer mixing region. Note that the peak RMS pressure fluctuation was three times lower than for transitional jet impingement. Past impingement, the near-wall $\langle uu \rangle$ increased with distance downstream, and attained a maximum at $x/D_h = 3.0$. This location corresponded well with the reduction in the rising slope in Nu_{loc} towards the secondary peak $x/D_h \approx 3.2$. As with the transitional jet impingement, the downstream locations of gradients of near-wall $\langle uu \rangle$ and RMS surface pressure fluctuation were inversely related. Non-dimensional fluctuating velocity variance profiles at four locations between

$x/D_h = 1.75$ and 3.50 are shown in Fig. 9b. A comparison of Figs. 8b and 9b illustrates the differences between the development of turbulence in the inner and outer regions at the two nozzle spacings. It is clear that the peak $\langle uu \rangle$ in the near-wall region occurred at a location following the peak $\langle uu \rangle$ in the outer region for the potential-core impingement, in contrast to observations for the transitional jet impingement. The profiles of surface pressure fluctuation, outer- and near-wall $\langle uu \rangle$ strongly suggest that the enhancement resulting in the secondary peak in heat transfer is a consequence of the interaction of correlated turbulent motion in the outer region and streamwise turbulence in the near-wall region.

Lytle and Webb [7] presented turbulence intensity and heat transfer measurements for circular air jets at $Y_n/D_h < 0.5$. They observed that the location of peak near wall $\langle uu \rangle$ (recorded at $y/D_h = 0.05$ for $Re = 7800$, and at $y/D_h = 0.025$ for $Re = 13,000$) corresponded well with that of secondary peak in heat transfer. They concluded that this secondary peak in local heat transfer coefficient at low spacings was a result of significantly higher turbulence in the boundary layer, which resulted from the intense shear in the outer region between the radially exiting jet and the stagnant ambient. While the turbulence data reported by Lytle and Webb corresponded to low nozzle-to-surface spacings, where a secondary peak in heat transfer coefficient was observed, in the present study, a similar peak in near-wall turbulence also occurred in the developing flow past impingement for transitional slot jet impingement. At such spacing, however, the origin of high near-wall turbulence intensity could not be related to turbulence in the outer region, and to a corresponding secondary heat transfer peak. It is important to note that for potential-core jet impingement, the location of peak near-wall turbulence intensity in both Lytle and Webb's and the present study corresponded well with the location of the reduction in slope of heat transfer coefficient towards the secondary peak, which suggested that the peak near-wall turbulence intensity marked a transition to a zero pressure gradient turbulent boundary layer.

Temporal wall temperature fluctuations, recorded at $x/D_h = 1.67$ and 3.2 for $Y_n/D_h = 0.5$ jet impingement, corresponding closely to the locations of the minimum and secondary peak in Nu_{loc}, respectively, are presented in Narayanan [16]. The time traces indicated a warm (compared to the mean surface temperature) thermal streak at both locations. As mentioned previously, such streaks were not observed at the impingement region. The observation of thermal streaks in the spanwise direction at $x/D_h = 1.67$ (and corresponding high RMS surface pressure and temperature fluctuations) and the rise in Nu_{loc} indicated that the correlated turbulence in the outer region caused an unsteadiness in the thermal boundary layer upon disappearance of strong mean favorable pressure gradient. The origin of the streamwise thermal streaks, indicating the presence of streamwise vortices, is unclear. Recently, Meola et al. [30] proposed that a separation and reattachment mechanism caused the non-monotonic trend in heat transfer coefficient at low nozzle-to-surface spacing in circular jet impingement. Although an intermittent separation and reattachment mechanism is also strongly suggested by data presented here, further studies are needed to verify this hypothesis.

Popiel and Trass [11] performed smoke-wire flow visualization on circular jet impingement at $Y_n/D_h = 1.2$, in which they observed that toroidal vortices, convected from the free jet shear region to the outer region of the wall-bounded flow, impinged on the wall (past the near-wall accelerated flow region). By placing the smoke-wire very close to the wall, they discovered the presence of ring-shaped wall eddies that rolled up on the plate surface between the large-scale toroidal vortices rotating counter to them. They hypothesized that these wall eddies, induced by the large-scale vortices impinging on the surface, caused the enhancement in heat and mass transfer rates leading to the secondary peak.

5. Conclusions

Flow field, surface pressure, and heat transfer rates associated with transitional and potential-core slot jet impingement was studied experimentally. Mean velocity and fluctuating velocity variance were determined using 1-D LDA, mean and RMS surface pressure fluctuations using a piezoresistive transducer, and surface temperatures using IR thermography.

For the transitional jet impingement, mean and RMS-averaged fluctuating surface pressure, and local heat transfer coefficient peaked in the impingement region and decreased monotonically in the wall-bounded flow past impingement. Generation of turbulence near the surface prior to impingement and the presence of spanwise vortices in the stagnation region [16] indicated an increase in near-wall turbulence, and could be the main factors that enhanced heat transfer rate from the surface in the transitional jet compared to the potential-core jet impingement.

Past impingement, the RMS surface pressure fluctuation decreased monotonically and was uncorrelated with the high streamwise fluctuating velocity variance in the outer region at $x/D_h = 2.0$. Peak streamwise fluctuating velocity variance in the near-wall locations occurred prior to that in the outer shear region, suggesting that turbulence in the outer region did not contribute to an increase in near-wall turbulence. However, the gradients of RMS surface pressure fluctuation and near-wall streamwise fluctuating velocity variance were inversely related. A change in the slope of the heat transfer coefficient profile at around $x/D_h = 1.5$ corresponded to the

end of the relation between surface pressure fluctuations and near-wall $\langle uu \rangle$, and indicated a transition from a favorable to a zero pressure gradient hydrodynamic and thermal boundary layer.

For potential-core jet impingement, the primary peak in heat transfer, which occurred in the impingement region, was followed by a region of local minimum and a secondary peak that occurred at around 1.5 and 3.2 hydraulic diameters from the jet centerline, respectively. The peak mean surface pressure occurred in the impingement region; however, the RMS-averaged surface pressure fluctuation profile exhibited a peak at a location of high outer region turbulence. There was a good correlation between the locations of the secondary peak in heat transfer and peak near-wall streamwise turbulence. However, local heat transfer coefficient could not be related solely to the near-wall streamwise turbulence, and was strongly dependent on the relation between outer shear layer and near-wall turbulence. Similar to the transitional jet impingement, the gradients of RMS surface pressure fluctuation and near-wall streamwise fluctuating velocity variance were inversely related. While the origin of high RMS pressure fluctuation for transitional jet impingement was attributed to the high turbulence near the stagnation region of the impinging jet, for the potential-core jet impingement, it resulted from correlated turbulent motion in the outer region of the wall-bounded flow past impingement. Past $x/D_h = 1.5$, the observation of thermal streaks (and corresponding high RMS surface temperature fluctuation) [16] and an increase in Nu_{loc} indicated that the correlated outer region turbulence caused an unsteadiness in the thermal boundary layer upon disappearance of strong mean favorable pressure gradient.

Acknowledgements

The authors acknowledge the financial support provided by the Texas A&M University Drying Research Center. VN would like to thank Dr. Stephen Danczyk and Prof. G.L. Morrison for insightful discussions and help with the set-up of the LDA system.

References

[1] H. Martin, Heat and mass transfer between impinging gas jets and solid surfaces, Adv. Heat Transfer 13 (1977) 1–60.
[2] R. Gardon, J.C. Akfirat, The role of turbulence in determining the heat-transfer characteristics of impinging jets, Int. J. Heat Mass Transfer 8 (1965) 101–108.
[3] S. Yokobori, N. Kasagi, M. Hirata, N. Nishiwaki, Role of large-scale eddy structure on enhancement of heat transfer in stagnation region of two-dimensional, submerged, impinging jet, in: Proceedings of the Sixth International Heat Transfer Conference, Toronto, Canada, 1978, pp. 305–310.
[4] C.D. Donaldson, R.S. Snedeker, A study of free jet impingement. Part 1. Mean properties of free and impinging jets, J. Fluid Mech. 45 (2) (1971) 281–319.
[5] C.D. Donaldson, R.S. Snedeker, D.P. Margolis, A study of free jet impingement. Part 2. Free jet turbulent structure and impingement heat transfer, J. Fluid Mech. 45 (3) (1971) 477–512.
[6] C.J. Hoogendoorn, The effect of turbulence on heat transfer at a stagnation point, Int. J. Heat Mass Transfer 20 (1977) 1333–1338.
[7] D. Lytle, B.W. Webb, Air jet impingement heat transfer at low nozzle-plate spacing, Int. J. Heat Mass Transfer 37 (12) (1994) 1687–1697.
[8] S. Yokobori, N. Kasagi, M. Hirata, M. Nakamura, Y. Haramura, Characteristic behaviour of turbulence and transport phenomena at the stagnation region of an axisymmetrical impinging jet, in: Proceedings of the 2nd Symposium on Turbulent Shear Flows, Imperial College, London, 1979, pp. 4.12–4.17.
[9] J. Sakakibara, K. Hishida, M. Maeda, Vortex structure and heat transfer in the stagnation region of an impinging plane jet (Simultaneous measurements of velocity and temperature fields by digital particle image velocimetry and laser-induced fluorescence), Int. J. Heat Mass Transfer 40 (13) (1997) 3163–3176.
[10] R.J. Goldstein, A.I. Behbahani, K.K. Heppelmann, Streamwise distribution of recovery factor and the local heat transfer coefficient to an impinging circular air jet, Int. J. Heat Mass Transfer 29 (8) (1986) 1227–1235.
[11] C.O. Popiel, O. Trass, Visualization of a free and impinging round jet, Exp. Thermal Fluid Sci. 4 (3) (1991) 253–261.
[12] M.D. Fox, M. Kurosaka, L. Hedges, K. Hirano, The influence of vortical structures on the thermal fields of jets, J. Fluid Mech. 255 (1993) 447–472.
[13] R. Viskanta, Heat transfer to impinging isothermal gas and flame jets, Exp. Thermal Fluid Sci. 6 (1993) 111–134.
[14] M. Korger, F. Krizek, Mass-transfer coefficient in impinging flow from slotted nozzles, Int. J. Heat Mass Transfer 9 (1966) 337–344.
[15] J. Zhe, V. Modi, Near wall measurements for a turbulent impinging slot jet, J. Fluids Eng. 123 (2001) 112–120.
[16] V. Narayanan, 2003, Time-resolved thermal flow structures in impinging slot jet flows, HT2003-47493, in: Proceedings of the 2003 Summer Heat Transfer Conference, Las Vegas, Nevada.
[17] S.E. Logan, A laser velocimeter for reynolds stress and other turbulence measurements, AIAA J. 10 (7) (1972) 933–935.
[18] G.L. Morrison, private communication, May 2001.
[19] R. Siegel, J.R. Howell, Thermal Radiation Heat Transfer, third ed., Hemisphere Publishing Corporation, Washington, DC, 1992, p. 1040.
[20] R.J. Moffat, Describing uncertainties in experimental results, Exp. Thermal Fluid Sci. 1 (1988) 3–17.
[21] C. Gau, C.C. Lee, Impingement cooling flow structure and heat transfer along rib-roughened walls, Int. J. Heat Mass Transfer 35 (11) (1992) 3009–3018.
[22] N. Rajaratnam, Turbulent Jets, in: Developments in Water Science, vol. 5, Elsevier Publishing Company, New York, NY, 1976.

[23] H. Tennekes, J.L. Lumley, A First Course in Turbulence, first ed., MIT press, Cambridge, MA, 1972, p. 75 (sixteenth printing).
[24] Y. Guo, D.H. Wood, Measurements in the vicinity of a stagnation point, Exp. Thermal Fluid Sci. 25 (2002) 605–614.
[25] V. Narayanan, An experimental flow field and heat transfer study of submerged double-sided reattachment and two-dimensional impingement slot jets, Ph.D. Dissertation, Texas A&M University, College Station, Texas, 2001.
[26] W.M. Kays, M.E. Crawford, Convective Heat and Mass Transfer, third ed., McGraw-Hill, Inc., Hightstown, NJ, 1993.
[27] C.V. Tu, D.H. Wood, Wall pressure and shear stress measurements beneath an impinging jet, Exp. Thermal Fluid Sci. 13 (1996) 364–373.
[28] J. Sakakibara, K. Hishida, W.R.C. Phillips, On the vortical structure in a plane impinging jet, J. Fluid Mech. 434 (2001) 273–300.
[29] K. Kataoka, Y. Kamiyama, S. Hashimoto, T. Komai, Mass transfer between a plane surface and an impinging turbulent jet: the influence of surface-pressure fluctuations, J. Fluid Mech. 119 (1982) 91–105.
[30] C. Meola, G. Cardone, C. Carmicino, G.M. Carlamagno, Fluid dynamics and heat transfer in an impinging air jet, in: G.M. Carlomagno, I. Grant (Eds.), Proceedings of the 9th International Symposium on Flow Visualization, Heriot-Watt University, Edinburg, Scotland, paper number 429, 2000, CD-ROM.
[31] Y. Becko, Impingement Cooling—A Review, in: Von Karman Lecture Series 83, Brussels, Belgium, 1976, pp. 1–40.
[32] P. Hrycak, Heat transfer from impinging jets, a literature review, Final report AFWAL-TR-81, Air Force Wright Aeronautical Laboratories, Wright-Patterson Air-Force Base, Ohio, 1981.
[33] M.K. Looney, J.J. Walsh, Mean-flow and turbulent characteristics of free and impinging jet flows, J. Fluid Mech. 147 (1984) 397–429.
[34] S.J. Downs, E.H. James, Jet impingement heat transfer—a literature survey, in: Proceedings of the National Heat Transfer Conference, Pittsburgh, Pennsylvania, 1987.
[35] S. Polat, Heat and mass transfer in impingement drying, Dry. Technol. 11 (6) (1993) 1147–1176.
[36] R. Gardon, J.C. Akfirat, Heat transfer characteristics of impinging two-dimensional air jets, J. Heat Transfer 86 (1966) 101–108.
[37] S. Belatos, N. Rajaratnam, Plane turbulent impinging jets, J. Hydraul. Res. 11 (1973) 29–59.
[38] E. Gutmark, M. Wolfshtein, I. Wygnanski, The plane turbulent impinging jet, J. Fluid Mech. 88 (4) (1978) 737–756.
[39] S.A. Striegl, T.E. Diller, The effect of entrainment temperature on jet impingement heat transfer, J. Heat Transfer 106 (1984) 27–33.
[40] K. Kataoka, M. Suguro, H. Degawa, K. Maruo, I. Mihata, The effect of surface renewal due to large-scale eddies on jet impingement heat transfer, Int. J. Heat Mass Transfer 30 (3) (1987) 559–567.
[41] K. Kataoka, Impingement heat transfer augmentation due to large scale eddies, Heat Transfer 1 (1990) 255–273.
[42] C. Gau, C.M. Chung, Surface curvature effect on slot-air-jet impingement cooling flow and heat transfer process, J. Heat Transfer 113 (1991) 858–864.
[43] C.S. McDaniel, B.W. Webb, Slot jet impingement heat transfer from circular cylinders, Int. J. Heat Mass Transfer 43 (2000) 1975–1985.
[44] A.H. Bietelmal, M.A. Saad, C. Patel, The effect of inclination on the heat transfer between a flat surface and an impinging two-dimensional air jet, Int. J. Heat Fluid Flow 21 (2000) 156–163.
[45] M. Choi, H.S. Yoo, G. Yang, J.S. Lee, D.K. Sohn, Measurements of impinging flow and heat transfer on a semi-circular concave surface, Int. J. Heat Mass Transfer 43 (2000) 1811–1822.
[46] S. Maurel, C. Solliec, A turbulent plane jet impinging nearby and far from a flat plate, Exp. Fluids 31 (6) (2001) 687–696.